Title

Regional variation in histopathologic features of tumor specimens from treatment-naive glioblastoma correlates with anatomic and physiologic MR Imaging

Journal

Neuro-Oncology, 14(7)

ISSN

1522-8517

Authors

Barajas, Ramon F
Phillips, Joanna J
Parvataneni, Rupa
et al.

Publication Date

2012-07-01

DOI

10.1093/neuonc/nos128

Peer reviewed

Neuro-Oncology 14(7):942–954, 2012.
doi:10.1093/neuonc/nos128

Regional variation in histopathologic features of tumor specimens from treatment-naive glioblastoma correlates with anatomic and physiologic MR Imaging

Ramon F. Barajas Jr, Joanna J. Phillips, Rupa Parvataneni, Annette Molinaro, Emma Essock-Burns, Gabriela Bourne, Andrew T. Parsa, Manish K. Aghi, Michael W. McDermott, Mitchel S. Berger, Soonmee Cha, Susan M. Chang, and Sarah J. Nelson

Department of Radiology and Biomedical Imaging (R.F.B., R.P., E.E.-B., G.B., S.C., S.J.N.); Department of Pathology (J.J.P.); Department of Neurological Surgery, University of California, San Francisco, California (A.M., A.T.P., M.K.A., M.W.M., M.S.B., S.C., S.M.C.)

Histopathologic evaluation of glioblastoma multiforme (GBM) at initial diagnosis is typically performed on tissue obtained from regions of contrast enhancement (CE) as depicted on gadolinium-enhanced, T1-weighted images. The non-enhancing (NE) portion of the lesion, which contains both reactive edema and infiltrative tumor, is only partially removed due to concerns about damaging functioning brain. The purpose of this study was to evaluate histopathologic and physiologic MRI features of image-guided tissue specimens from CE and NE regions to investigate correlations between imaging and histopathologic parameters. One hundred nineteen tissue specimens (93 CE and 26 NE regions) were acquired from 51 patients with newly diagnosed GBM by utilizing stereotactic image-guided sampling. Variables of anatomic, diffusion-weighted imaging (DWI), and dynamic susceptibility–weighted, contrast-enhanced perfusion imaging (DSC) from each tissue sample location were obtained and compared with histopathologic features such as tumor score, cell density, proliferation, architectural disruption, hypoxia, and microvascular hyperplasia. Tissue samples from CE regions had increased tumor score, cellular density, proliferation, and architectural disruption compared with NE regions. DSC variables such as relative cerebral blood volume, peak height, and recovery factor were significantly higher, and the percentage of signal intensity recovery was significantly lower in the CE compared with the NE regions. DWI variables were correlated with histopathologic features of GBM within NE regions. Image-guided tissue acquisition and assessment of residual tumor from treatment-naive GBM should be guided by DSC in CE regions and by DWI in NE regions.

Keywords: dynamic susceptibility contrast-enhanced imaging, diffusion-weighted imaging, glioblastoma, image-guided tissue acquisition, magnetic resonance imaging.

Glioblastoma multiforme (GBM) is the most common and aggressive primary brain tumor in adults and demonstrates heterogeneous imaging characteristics, histologic features, and clinical outcomes. Despite significant advances in targeted surgical resection and conformal radiation therapy, GBM remains a uniformly deadly disease with a dismal prognosis of less than 10% 2-year overall survival.[1–6] The presence of infiltrative tumor makes it difficult to define tumor margins, as regions with malignant features are intermingled within functioning brain that cannot be removed without severe detriment to the patient. Although it may be possible to achieve a gross total resection of the contrast-enhanced (CE) component of the lesion, there is often a substantial non-enhancing (NE) tumor component that is left behind and eventually becomes the site of focal recurrence.

The current standard for diagnosis and evaluation of prognosis for GBM remains histopathologic analysis of

Received February 13, 2012; accepted April 18, 2012.

Corresponding Author: Sarah J. Nelson, PhD, University of California, San Francisco, Department of Radiology and Biomedical Imaging, Mission Bay, Byers Hall, Room BH-303, MC 2532, 1700 4th Street, San Francisco, CA 94158-2330 (sarah.nelson@ucsf.edu).

tumor specimens. The World Health Organization II diagnostic criteria of GBM are based upon the presence of microvascular hyperplasia, cellular proliferation, nuclear atypia, architectural disruption, and necrosis.[3–6] Tissue samples are typically obtained from the CE component of the tumor.[5–7] There is rarely an examination of heterogeneity throughout the entirety of the lesion or an attempt to make direct correlations between imaging and histopathologic features. The introduction of MRI sequences that provide tissue contrast based upon physiologic parameters, such as diffusion-weighted imaging (DWI) and T2* dynamic susceptibility–weighted, contrast-enhanced perfusion imaging (DSC), holds significant promise for identifying characteristics of GBM that are representative of biologic behavior.[7–25] However, there remains the need to understand the relationship of these physiologic imaging measures with standard anatomic imaging parameters and histopathologic characteristics so they can collectively be utilized to assess tumor burden.[7–10]

DWI-derived apparent diffusion coefficient (ADC) and fractional anisotropy (FA) values are increasingly utilized in the evaluation of patients with brain tumors, as these quantitative measures can be obtained in less than 5 min. ADC and FA values have been previously associated with increased cell density and disruption of normal tissue architecture.[26–29] Recent studies investigating tissue samples from patients with primary CNS lymphoma have suggested that there is an inverse correlation between ADC values and cell density,[28,29] but similar studies involving specimens from GBM have yielded varied results.[29–32]

DSC MRI has been widely used to investigate variations in cerebral blood volume (CBV), peak height (PH), recovery factor (RF), and percentage of signal intensity recovery (PSR).[8–15] Prior investigations have shown that DSC provides quantitative parameters that reflect hemodynamic characteristics of normal and tumor microvasculature within the brain and have demonstrated its clinical utility as a companion to anatomic MRI differentiating GBM from single brain metastasis,[8–18] predicting glioma grade,[18–21] and distinguishing recurrent brain tumors from radiation necrosis.[33–36]

The purpose of the current study was to determine whether the differential distribution of histologic features between tissue specimens that were obtained from CE and NE regions of tumor in patients with treatment-naive GBM is associated with specific anatomic and physiologic MRI parameters. This investigation utilized image-guided tumor specimens from patients undergoing initial surgical resection in conjunction with a battery of histopathologic tests in order to make direct correlations between their biologic features and the corresponding in vivo MRI parameters.

Methods

Patient Population

A total of 51 adult patients (35 men, 16 women; mean age 64.5 y, range 33–85) with newly diagnosed GBM were prospectively enrolled into our study from July 2007 to June 2010. The study was in compliance with the University of California San Francisco Health Insurance Portability and Accountability Act, our institutional review board and Committee on Human Research, and the ethical human-subject standards of the World Medical Association Declaration of Helsinki: Research. Written informed consent was obtained from all patients.

Preoperative Imaging Protocol

Forty-six patients underwent preoperative anatomic and physiologic MRI using a 3T MR scanner (GE Medical Systems), and 5 patients were imaged on a 1.5T Signa Horizon scanner (GE Medical Systems). Similar MRI protocol was utilized: 3 plane localizer (8.5 ms repetition time [TR]/1.6 ms echo time [TE]), sagittal T1-weighted spin echo (600 ms/17 ms TR/TE), axial 3D T2-weighted fast spin echo (FSE) (3000 ms/102 ms TR/TE), axial fluid-attenuated inversion recovery (FLAIR; 10 000 ms/148 ms/2200 ms TR/TE/inversion time), axial DWI (echo-planar; 10 000 ms/99 ms TR/TE; 3 mm/0 mm slice thickness/interslice gap; 256×256 matrix size; 24 cm field of view; 6 gradient directions, $b = 0$ and 1000 s/mm^2), and contrast-enhanced 3D spoiled gradient-recalled acquisition in the steady state (SPGR) T1-weighted (34 ms/8 ms TR/TE; 1.5 mm/0 mm, slice thickness/interslice gap) and T1-weighted postcontrast spin echo images (600 ms/17 ms TR/TE). In selected cases, data from 3D H-1 MR spectroscopic imaging (MRSI) were acquired for evaluation of tumor metabolism and contributed to the site selection for obtaining tissue samples that were likely to represent tumor, based upon the choline to *N*-acetyl aspartate index (CNI) being >2 SEs above normal.[11,37,38]

Axial DSC was performed utilizing a series of T2* gradient-echo echo-planar images (flip angle = 35° or 60°; 54–56/1250–1500 ms TE/TR; 128×128 matrix size; 26×26 cm field of view; 8–12 slices, 3–4 mm slice thickness) acquired immediately before, during, and after (total of 60–80 time points) intravenous administration of 0.1 mmol/kg gadopentetate dimeglumine (Gd-DTPA; Magnevist, Bayer HealthCare Pharmaceuticals) with an MR-compatible power injector (Medrad, Spectris Solaris) at a rate of 4–5 mL/s through a 20-gauge angiocatheter, followed by 20 mL of continuous saline flush. The first 10 echo-planar imaging acquisitions were performed before the injection of Gd-DTPA to establish a precontrast baseline. The region selected for DSC coverage included the entire tumor volume as determined by T2-weighted FLAIR and FSE images. A TE of 54 ms and flip angle of 35° were selected to maximize the effect of susceptibility changes while minimizing T1 effect during the first pass of the contrast agent.

Physiologic MRI Processing

MR imaging data were transferred to a commercially available Linux workstation were data from postcontrast T1-weighted images in 3D SPGR images,

T2-FLAIR images, DSC, DWI, and, where available, H-1 MRSI. At the workstation, these sequences were processed and co-registered as described previously.[39] The accuracy of co-registration was manually verified by visual inspection.

DSC and DWI analysis was performed using software developed by our group.[13,39,40] The T2* dynamic signal intensity time curves acquired during the first pass of the gadolinium bolus were converted into dynamic ΔR2* curves and resampled to match the spatial resolution of the anatomic imaging series. PH was defined as the maximum ΔR2* value of the first-pass curve. PSR was calculated as the difference between the PH value and the average values of the final 5 time points in the dynamic ΔR2* series divided by the PH value. CBV and RF maps were calculated on a voxel-by-voxel basis utilizing a modified gamma-variate function that takes into account leakage of the contrast agent.[13,39,40] DWI was used for the production of ADC and FA maps on an automated voxel-by-voxel basis. Several of the physiologic MRI parameters were normalized by dividing the estimated values in normal-appearing white matter from the contralateral hemisphere before comparison with the histologic data (rCBV, rPH, rADC, rFA).

Preoperative Tumor Tissue Site Selection and MRI Analysis

Anatomic and physiologic MRI was used to guide the prospective selection of tissue sampling sites within the T2 FLAIR and FSE hyperintense portion of the tumor. Tissue sampling sites were preoperatively planned and marked on the anatomic images that were used by the surgical navigation workstation (Brainlab, VectorVision Navigation System; Medtronic, Stealth Station). Criteria used to plan sites were based upon results from previous studies as having either rPH > 3, ADC < 1200, or, when MRSI data were available, CNI > 2.[13,18,31,32,37,38,41,42] The tissue targets were marked on the anatomic images to be used by the surgeon for intraoperative sample localization. Requested tissue sampling sites were obtained more than 85% of the time with at least one requested tissue sampling site for all patients being sampled; however, it was not always possible to match all the requested tissue targets, so the actual locations of the acquired tissue sample were saved on the surgical navigational system as both screenshots and as a list of image coordinate values. The tissue coordinates were subsequently used to define spherical regions of interest (ROIs) of 5 mm diameter and to record corresponding values of anatomic and physiologic MRI parameters. Accurate co-registration of intraoperatively generated screen shots that defined the tumor specimen site and the corresponding ROI were reviewed by a neuroradiologist who was blinded to other patient data. The median intensity values for each of the relevant imaging parameters within the sample ROIs were determined for the subsequent imaging analysis using automated software developed in our research group.

Intraoperative Tissue Collection and Histopathologic Tumor Analysis

After removal from the brain, tissue specimens were divided in half, with one half snap frozen in liquid nitrogen for potential future studies and the other half immediately placed in zinc-formalin for 4–6 h, dehydrated in a series of graded alcohols, and infiltrated with low-temperature paraffin for histologic analysis. Sections from the tissue specimens were stained with hematoxylin and eosin (H&E) or immunostained using an automated immunohistochemical (IHC) tissue staining process (Ventana Medical Systems Benchmark XT). Digital images were captured with an Olympus BX41TF microscope and an Olympus DP70 digital microscope camera.

For each tissue specimen, the presence of tumor cells was scored based upon review of H&E-stained sections by a neuropathologist as 0 = no tumor present, 1 = infiltrating tumor margin, 2 = infiltrating cellular tumor, and 3 = highly cellular infiltrating tumor involving $>75\%$ of the tissue. Tumor cells were identified based upon morphologic features, including cytologic atypia, enlarged nuclear to cytoplasmic volume ratio, and hyperchromasia. The cumulative extent of necrosis was scored as 0 = no necrosis, 1 = focal necrosis involving $<50\%$ of the tissue area, and 2 = extensive necrosis involving $\geq 50\%$ of the tissue area.

The degree of microvascular hyperplasia, hypoxia, and architectural disruption was qualitatively measured using IHC stained sections for factor VIII, carbonic anhydrase (CA)–9, and SMI-31, respectively, using an ordinal scale of immunoreactivity. For factor VIII staining, the presence of specific microvascular elements was scored as 0 = delicate microvasculature only, 1 = simple hyperplastic structures identified (hyperplastic capillaries with definitive lumen), and 2 = complex microvascular hyperplasia (circumferential multilayered and glomeruloid-type vessels). The contribution of each type of microvascular element to the overall vascularity was scored as 0 = not present, 1 = present but not predominant, and 2 = predominant.

The degree of hypoxia, as denoted by percentage of CA-9 positivity of tissue, was scored as 0 = no positive staining, 1 = $<10\%$, 2 = $\geq 10\%$ but $<25\%$, and 3 = $\geq 25\%$. The CA-9 gene has a hypoxia-responsive element in its promoter, and its expression at the protein level is commonly used as a marker for hypoxia. To assess the degree of architectural disruption, we performed an IHC analysis with SMI-31, an antibody against a phosphorylated neurofilament epitope in thick and thin axons, and scored the samples based on the extent of SMI-31 staining as 0 = no disruption of the normal architecture, 1 = minimal disruption, 2 = mild disruption, and 3 = severe disruption with no residual SMI-31 immunostaining.

The total number of cells and the total number of Ki-67 stained cells was quantified in 3–5 separate fields at 20× magnification to assess total cell number and standardized proliferation index. A minimum of 400 nuclei were counted per sample. An attending neuropathologist with greater than 10 years experience

who was blinded to the results of MRI performed all quantitative and qualitative histopathologic assessments. All of the tissue specimens were of sufficient size and IHC staining quality to be included for analysis.

Statistical Analysis

There were 3 components to the analysis: (1) assessment of intratumor variation for each histopathologic and MRI variable, (2) assessment of whether MRI parameters (perfusion, diffusion, and anatomic) were predictive of GBM histopathology, and (3) evaluation of associations within histopathology features and in vivo MRI parameters.

Association of Histopathology Characteristics and MRI Variation within Tumor Specimen Regions.—Mixed effects modeling was performed to estimate the coefficient of intratumor variation (as measured in CE vs NE regions) for each histopathologic and MRI variable in the subset of patients who had tumor specimens from both regions. For each continuous variable, the initial model included a fixed effect for each tissue specimen site and a random effect for each patient. This model can be written as:

$$y_{ijk} = \beta_j + b_i + \varepsilon_{ijk}; \quad i = 1, \ldots, 51; \quad j = 1, 2; \quad k = 1, \ldots, k_i,$$

where y_{ijk} is the histopathologic or imaging value of the ith subject in the jth tumor specimen region for the kth biopsy; β_j is the tumor specimen–specific intercept; and ε is the residual. This model assumes that $b_i \sim N(0,\sigma_b^2)$ and $\varepsilon_{ijk} \sim N(0,\sigma^2)$. The assumptions of normality for the random effects were verified with quantile-quantile plots. For some histologic and MRI variables, plots of residuals against fitted values demonstrated heteroscedasticity within tumor specimen regions. In those cases, the model was adjusted to account for unequal variances within tumor specimen regions. Interactions between the fixed and random effects were also investigated. Models were pairwise compared and the coefficient/P value for the best model is reported. R and the Nonlinear Mixed Effects package were used for the continuous-value outcome mixed effect models.

To compare the ordinal histopathology variables between CE and NE tumor specimen regions, we employed a proportional odds logistic regression model with repeated measures to model the probability of observing a lower versus a higher response. This model is written as:

$$\text{logit}[P(Y_{ijk} \leq \kappa | X_i, Z_i)] = \alpha_k + x'_{ij}\beta + Z'_{ij}\beta + z'_{ij}b_i; \quad i = 1, \ldots, 35; \quad k = 1, \ldots, c-1,$$

where c is the total number of levels of the ordinal variable, X_i and Z_i are the design matrices for the fixed effects and for the random effects, respectively; x_{ij} and z_{ij} are rows corresponding to the jth biopsy region; and β and b_i are the vectors of the fixed and random parameters, respectively. The intercepts are fixed and category dependent. The odds ratio and P value for each variable is reported. The mixed effect models of ordinal-valued outcomes were analyzed with Proc Genmod in SAS v.9.2.

Predictive Ability of MRI Parameters by Tumor Specimen Region.—The primary analysis focused on whether anatomic, diffusion, or perfusion parameters (rT1C, rFSE, rFLAIR, rFA, rADC, rCBV, rPH, PSR, or RF) were predictive of malignant glioma histopathology as assessed in each region by tumor cellularity (H&E), proliferation (Ki-67), overall cell density (H&E), necrosis (H&E), microvascular hyperplasia (factor VIII), hypoxia (CA-9), architectural disruption (SMI-31), or microvascular morphology (delicate, simple, complex; factor VIII). Univariate mixed effects linear models fit as described above were used with each histopathology feature as the outcomes, and the imaging parameter was used as a fixed predictor adjusting for the patient effect. For models involving continuous outcomes, the coefficients were reported if they were statistically significant at $P \leq .05$ and if the within-tumor residual variance decreased at least 5% compared with the unconditional means model. Each association was also assessed by randomly selecting one sample per patient and calculating a Kendall's tau correlation coefficient (τ). This sampling process was repeated 100 times. A strong correlation was identified if the corresponding P value for τ was significant at $P \leq .05$ in 70% of the 100 samples. The median τ and P value are reported where a correlation did not exist linearly. Imaging parameters statistically significant at $P \leq .15$ were modeled pairwise with and without interaction. These models were compared with the univariate model to confirm whether the additive effect strengthened the model.

Associations among Histopathology Scores and MRI by Tumor Specimen Region.—Exploratory associations were estimated within histopathology features and within in vivo MRI parameters stratified by tissue sample regions. Univariate mixed effects linear models were fit as described above. Only associations of the following MRI variables are summarized: rT1c, rFSE, rFLAIR, rCBV, rADC, and rFA. Hypoxia, necrosis, and complex vessel scores were excluded from analyses involving NE regions because there were a relatively small number of nonzero values.

Results

A total of 119 image-guided tissue specimens were obtained from regions of suspected tumor during surgical resection of 51 patients who were assessed as having newly diagnosed GBM. Ninety-three tissue specimens were obtained from CE regions and 26 from NE regions. The analysis of DSC data was limited to patients ($N = 35$) imaged with a flip angle of 35° to minimize T1 signal intensity effects during the first pass of the contrast agent (N tissue samples = 72).

Differential Distribution of Histopathologic Features within CE and NE Regions

Summary statistics for regional histopathology features obtained from this cohort are presented in Table 1 and Fig. 1. Tumor was found in 81% of NE tissue specimens and 90% of CE tissue specimens. Considering that the surgeon was not always able to sample the requested location, the high tumor identification rate indicated that the imaging criteria used for tumor targeting were highly effective. Tissue specimens obtained from CE regions had significantly increased tumor score ($P = .04$) and architectural disruption as demonstrated by SMI-31 ($P = .05$) compared with NE regions. Proliferation and tumor cell density were also found to be elevated within CE regions (proliferation mean 15.8% vs 4.6%, $P = .04$; tumor cell density mean 268 vs 146, $P = .007$). The relative contribution of delicate vascular morphology was higher in NE tumor tissue regions ($P = .01$). As is shown in Fig. 1, there were relatively few samples from NE regions with complex microvascular hyperplasia, hypoxia, and necrosis (19%, 4%, and 0%, respectively).

Differential Distribution of MRI Parameters within CE and NE Regions

Summary statistics for regional anatomic and physiologic MRI values obtained from this cohort are summarized in Table 2 and Fig. 2. Compared with NE regions, tissue specimens obtained from CE regions demonstrated significantly higher levels of rT1C, rFSE, rCBV, rPH, and RF ($P < .01$). As expected, PSR was found to be significantly lower within CE regions compared with NE

Table 1. Regional histopathological summary statistics and differential regional expression[a]

Categorical Features

Histologic Value	Tissue Region	Pt #	TS #	Frequency Distribution (%)				Random Effect Model Analysis				
				0	1	2	3	# Pairs	Odds Ratio	95% Confidence Interval		*P* Value
Tumor score	NE	20	26	19	35	27	19	16	2.6	1.1	6.6	.04
	CE	47	90	10	18	28	44					
Necrosis	NE	20	26	100	0	0	NA	17	NA	NA	NA	NA
	CE	48	92	69	22	9	NA					
Hypoxia	NE	20	26	96	0	0	4	16	NA	NA	NA	NA
	CE	47	89	45	17	18	22					
AD	NE	20	26	35	31	23	12	16	2.8	1	7.7	.05
	CE	46	88	17	19	22	42					
Total MVH	NE	20	26	35	46	19	NA	16	2.5	1	6.2	.06
	CE	47	89	22	44	34	NA					
Delicate MVH	NE	20	26	4	15	19	62	16	0.3	0.1	0.8	.01
	CE	47	89	18	3	25	27					
Simple MVH	NE	20	26	31	35	15	19	16	2	0.8	5.2	.15
	CE	47	89	18	26	26	30					
Complex MVH	NE	20	26	81	11	8	0	16	NA	NA	NA	NA
	CE	47	89	60	16	10	14					

Continuous Features

Histologic Value	Tissue Region	Pt #	TS #	Min	Median	Max	SD	# Pairs	B	95% Confidence Interval		*P* Value
Proliferation	NE	20	26	0.0	4.6	26.7	7.3	16	5.9	0.2	11.6	.043
	CE	47	89	0.0	15.8	59.2	13.9					
Tumor cell number	NE	20	26	66.5	145.5	474	88.7	17	103	30.6	175.1	.007
	CE	48	91	43.0	267.8	921	165.9					

Abbreviations: Pt #, number of patients; TS #, number of tissue samples; NA, not applicable; AD, architectural disruption; MVH, microvascular hyperplasia; SD, standard deviation; B, β coefficient.

[a]Regional summary statistics of histopathologic values obtained from contrast-enhancing (CE) and non-enhancing (NE) regions are presented. The estimated difference in effect between the 2 regions (NE as baseline) is summarized by the odds ratio/*P* value from a random effects model. Tumor score: 0 = no tumor present; 1 = infiltrating tumor margin; 2 = infiltrating cellular tumor; 3 = highly cellular infiltrating tumor involving >75% of the tissue. Necrosis: 0 = no necrosis; 1 = focal necrosis involving <50% of the tissue area; 2 = extensive necrosis involving ≥50% of the tissue area. Hypoxia = 0, no positive staining; 1 = <10% of the tissue; 2 = ≥10% of the tissue but <25%; 3 = ≥25% of the tissue is CA-9 positive. AD: 0 = no disruption of the normal architecture; 1 = minimal disruption; 2 = mild disruption; 3 = severe disruption with no residual SMI-31 immunostaining. Total MVH: 0 = delicate microvasculature only; 1 = simple hyperplastic structures identified (hyperplastic capillaries with definitive lumen); 2 = complex microvascular hyperplasia (circumferential multilayered and glomeruloid-type vessels). Relative contribution of each vascular morphology (delicate, simple, complex) to total vascularity within the sample: 0 = no contribution; 1 = minimal; 2 = prevalent; 3 = predominant. Proliferation is based on total number of Ki-67-positive cells relative to total number of cells in 3–5 separate fields at 20× magnification. Tumor cell number: total cells per field at 200× magnification.

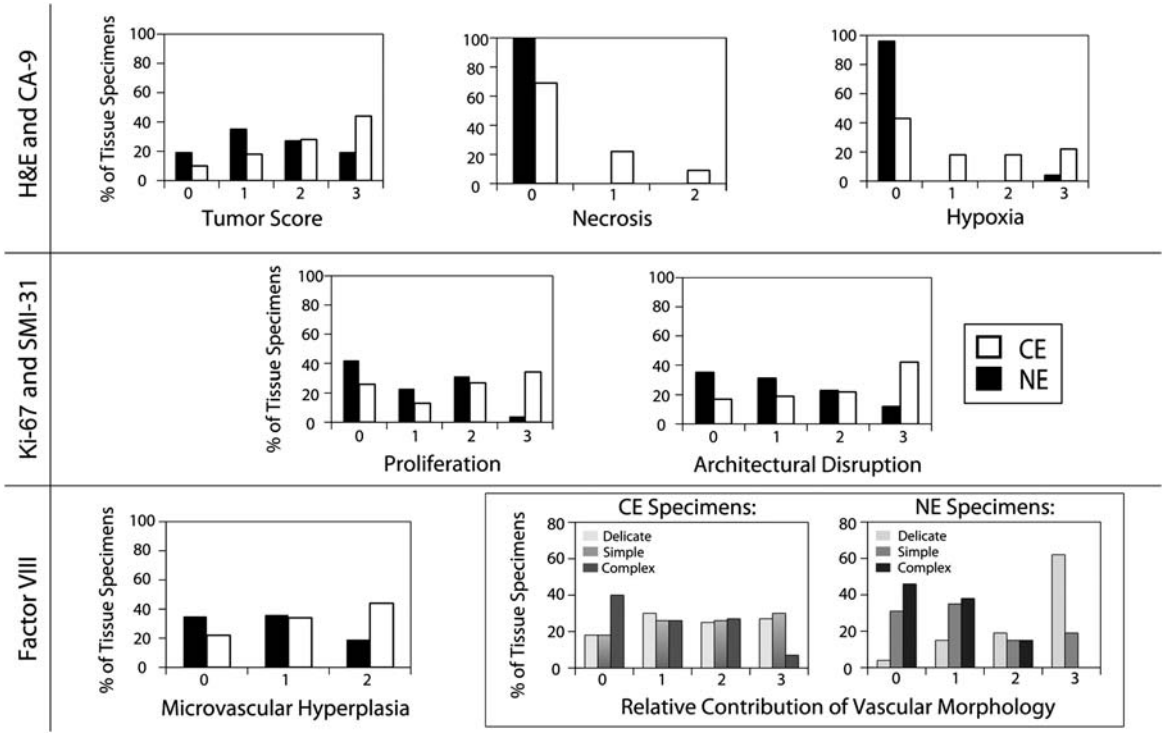

Fig. 1. Frequency distribution of histopathologic features of glioblastoma multiforme among contrast-enhancing and non-enhancing regions. Histopathologic features were noted to be heterogeneously distributed within both enhancing and non-enhancing regions. Bar graphs of the entire cohort's histopathological features demonstrate significantly increased distribution of tumor score, architectural disruption, and complex vascular hyperplasia morphology within contrast-enhancing regions compared with non-enhancing biopsy regions ($P < .05$). Delicate vascular morphology distribution was increased within non-enhancing biopsy regions compared with contrast-enhancing regions ($P = .01$). The distributions of overall vascular hyperplasia and simple microvascular hyperplasia morphology were not different between enhancing and non-enhancing regions. Hypoxia and pseudopalisading necrosis were not observed in non-enhancing regions.

regions ($P = .007$). The distributions of rADC, rFA, and rFLAIR were not found to be different between CE and NE regions.

Association of Histology and MRI Parameters within CE Tumor Regions

Table 3 summarizes the statistically significant associations between MRI and histopathology parameters in samples from CE tumor regions (detailed results are shown in Supplementary Table S1). Univariate mixed effects model analyses demonstrated that tumor score was associated with rFLAIR, rCBV, rPH, and RF ($P = .01$, .003, .011, and .015, respectively). Microvascular hyperplasia and proliferation were associated with rT1C, rCBV, and rPH ($P = .027$, .005, and .005, respectively; Fig. 3). Tumor cell density was associated with rCBV and rPH ($P = .01$). Necrosis was associated with rCBV ($P = .003$), and delicate vasculature was inversely associated with rT1C ($P = .033$). There were no significant univariate relationships observed between histopathologic features and PSR, rFSE, rADC, or rFA parameters within CE regions.

Pairwise models of rFLAIR with perfusion parameters rCBV (odds ratio [OR] = 2.38, $P = .10$), rPH (OR = 2.46, $P = .002$), or RF (OR = 0.85, $P = .044$) were predictive of tumor score. Additional pairwise predictive models of tumor score included RF with rCBV (OR = 2.26, $P = .003$) and RF with rPH (OR = 2.74, $P = .03$). Pairwise models of rT1C with rCBV (OR = 1.88, $P = .007$) and rT1C with rPH (OR = 2.43, $P = .002$) were predictive of microvascular hyperplasia.

Association of Histology and MRI Parameters within NE Tumor Regions

The associations between MRI and histopathologic features in NE regions are summarized on the right-hand side of Table 3 (detailed results are shown in Supplementary Table S2). Inverse associations were observed for tumor score with rFSE and rADC ($P = .03$ and .02) as well as proliferation with rFLAIR and rADC ($P = .01$; Fig. 4). Architectural disruption (SMI-31) was inversely related to rADC ($P = .005$; Fig. 4) but positively correlated to rFA and rPH ($P = .035$ and .038). Tumor cell density was associated with increasing rPH ($P = .05$), while delicate microvasculature was found to be positively associated with rT1C ($P = .03$) and rFA ($P = .009$).

Associations Among Histology Parameters

The potential interactions between histopathologic features within each tumor region are summarized in

Table 2. Regional anatomic and physiologic magnetic resonance imaging values: summary statistics and differential regional expression based on contrast enhancement or non-enhancement

MRI Value	Tissue Region	Summary Statistics						Mixed Effects Model				
		Pt #	TS #	Min	Median	Max	Std	Pair #	B	95% Confidence Interval		*P* Value
Anatomic												
rT1C	NE	20	26	0.60	0.92	1.42	0.21	17	0.4	0.2	0.7	.004
	CE	48	93	0.55	1.29	2.61	0.46					
rFSE	NE	20	26	0.94	1.57	4.36	0.92	17	0.7	0.2	1.3	.007
	CE	48	93	0.38	1.94	6.34	0.92					
rFLAIR	NE	20	26	0.71	1.42	2.35	0.37	17	0.1	−0.1	0.3	.569
	CE	48	93	0.83	1.50	2.94	0.41					
DSC												
rCBV	NE	11	15	0.47	1.64	2.77	0.70	7	0.9	0.4	1.4	.003
	CE	29	52	0.45	2.29	8.61	1.50					
rPH	NE	12	17	0.49	1.48	4.06	0.86	8	0.6	0	1.1	.046
	CE	30	53	0.27	1.67	6.74	1.08					
PSR	NE	12	17	77.5	94.5	99.5	5.9	8	−19.6	−31.9	−7.4	.007
	CE	30	53	34.5	78.5	96.5	16.9					
RF	NE	11	15	0.89	2.65	3.75	0.85	7	2.6	1.2	4	.002
	CE	29	52	0.37	3.60	13.15	3.01					
DWI												
rADC	NE	19	24	0.86	1.09	2.34	0.37	16	0.2	−0.1	0.5	.156
	CE	47	90	0.35	1.43	3.69	0.48					
rFA	NE	19	24	0.37	1.03	2.37	0.50	16	−0.2	−0.4	0.1	.224
	CE	47	90	0.21	0.68	2.50	0.36					

Abbreviations: CE, contrast-enhanced; NE, non-enhanced; MRI, magnetic resonance imaging; DWI, diffusion-weighted imaging; DSC, dynamic susceptibility–weighted, contrast-enhanced perfusion imaging; Std, standard deviation; rFLAIR, relative fluid-attenuated inversion recovery, T2 hyperintensity value; rT1C, relative T1 enhancing value; rFSE, relative fast spin echo T2 hyperintensity value; rCBV, relative cerebral blood volume; rPH, relative peak height; PSR, percentage of signal intensity receovery; RF, recirculation factor; rADC, relative apparent diffusion coefficient; rFA, relative fractional anisotropy; Min, minimum value within region of interest; Pt #, number of patients; TS #, number of tissue samples; Max, maximum value within region of interest. The estimated difference in effect between the 2 regions (NE as baseline) is summarized by the coefficient/*P* value from mixed effects models. Relative values indicated by the prefix *r* indicates tumor value divided by contralateral white matter value.

Table 4 (details shown in Supplementary Table S3). No assessment was made for complex microvascular morphology because the number of samples with positive scores was relatively small (41% for CE and 20% for NE regions). Within CE tissue specimens, all histopathologic features, except for delicate vasculature, were positively associated with tumor score, proliferation, and total microvascular hyperplasia. Delicate microvascular morphology was inversely associated with tumor score, proliferation, total microvascular hyperplasia, and necrosis within CE tissue specimens. Additionally, CE tissue specimens demonstrated positive associations among hypoxia, architectural disruption, simplex microvascular morphology, and necrosis.

Relationships among proliferation, microvascular hyperplasia, architectural disruption, and simplex vasculature scores were similar in NE tissue specimens—however, low numbers of positive scores for necrosis and hypoxia (0% and 4%, respectively) precluded evaluation of these features. NE tissue specimens lacked a significant association of delicate microvascular morphology with other histopathologic features and for tumor cell density with proliferation or microvascular hyperplasia.

Associations Among MRI Parameters

Associations among MRI parameters are summarized in Table 5 (details are shown in Supplementary Table S4). rFSE and rFLAIR were associated within CE and NE regions. rT1C was inversely associated with rFSE and rFLAIR only within NE regions. rCBV was positively associated with rPH and inversely associated with rADC in CE and NE regions. rCBV was associated with rT1C only in CE regions. rADC was positively associated with rFSE and inversely associated rFA in CE and NE regions. Similar parameters from the same imaging modality, such as rCBV and rPH, were positively related, and PSR was inversely related with RF for CE and NE regions.

Discussion

In this study we prospectively collected tissue specimens from CE and NE regions in patients with untreated GBM utilizing MRI-guided neurosurgical techniques to evaluate their physiologic MRI and histopathologic characteristics and to assess the correlation of in vivo

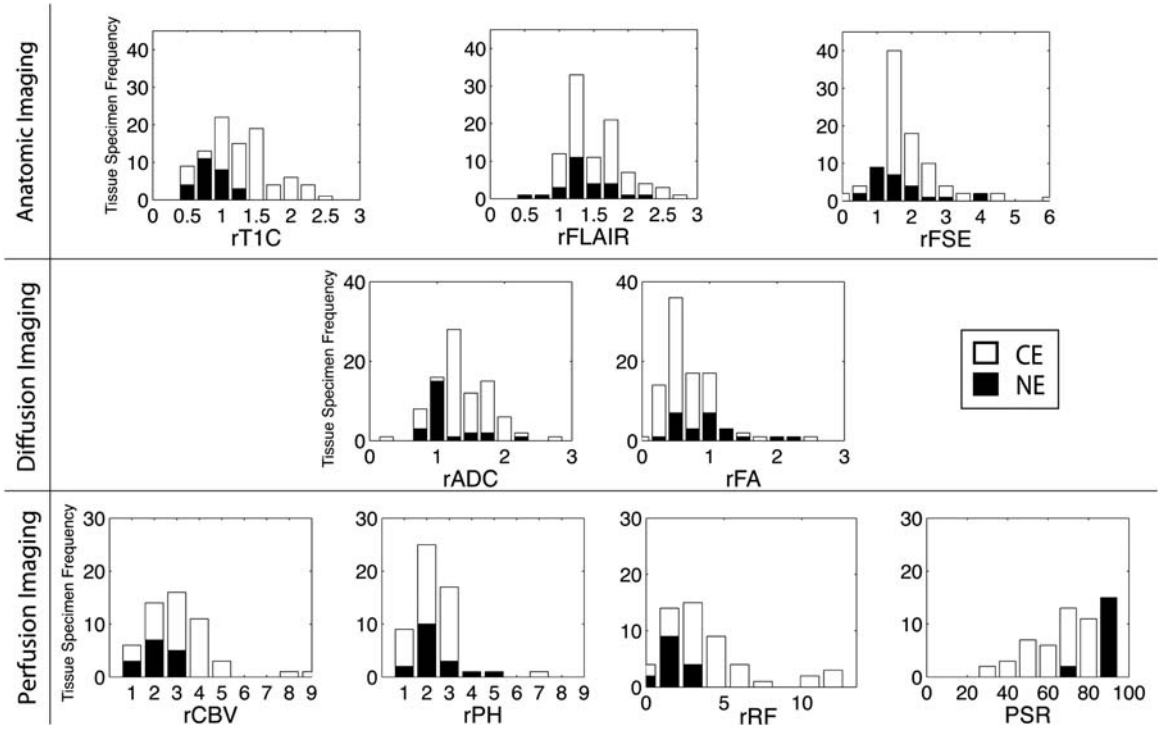

Fig. 2. Distribution of dynamic susceptibility–weighted, contrast-enhanced perfusion imaging (DSC) perfusion, diffusion, and anatomic T1- and T2-weighted magnetic resonance imaging (MRI) characteristics among contrast-enhancing (CE) and non-enhancing (NE) regions. Histograms as a distribution of the entire cohort's MRI values demonstrate significantly elevated relative T1 enhancing value (rT1C), relative fast spin echo T2 hyperintensity value (rFSE), relative cerebral blood volume (rCBV), relative peak height (rPH), and recirculation factor (RF) values within contrast-enhancing regions compared with non-enhancing regions ($P < .01$). Mean PSR values were significantly lower within contrast-enhancing regions compared with non-enhancing regions ($P < .01$). Relative apparent diffusion coefficient (rADC), relative fractional anisotropy (rFA), and relative fluid-attenuated inversion recovery T2 hyperintensity value (rFLAIR) were not observed to be differentially distributed between contrast-enhancing and non-enhancing regions.

Table 3. Associations among key histopathologic and in vivo magnetic resonance imaging parameters[a]

	CE Region								NE Region							
	rT1C	rFSE	rFLAIR	rCBV	rPH	RF	rADC	rFA	rT1C	rFSE	rFLAIR	rCBV	rPH	RF	rADC	rFA
Tumor score			−	+	+	−				−			+		−	
Proliferation	+			+							−				−	
Total MVH	+			+	+											
Delicate MVH	−								+							+
Simple MVH					+											
Necrosis				+												
TCN				+	+								+			
AD													+		−	+

Abbreviations: CE, contrast-enhancing; NE, non-enhancing; +, positive correlation; −, inverse correlation; MVH, microvascular hyperplasia; TCN, tumor cell number per high-power field; AD, architectural disruption.
[a]Statistical significance, $P < .05$. Total MVH denotes all microvascular hyperplasia, including both simple and complex. Tumor cell density denotes mean tumor cell number per 200× microscopic field. Tumor cell density denotes mean tumor cell number per 200× microscopic field.

MR parameters with histologic features of GBM. We observed that a number of histopathologic features and quantitative MRI parameters differ between CE and NE regions. These variables also demonstrate significant correlations suggesting that DSC perfusion and DW MRI are capable of detecting heterogeneous histopathologic features within anatomically distinct portions of treatment-naive GBM.

The results of our study suggest that the tissue sampling site criteria of either rCBV > 3, ADC < 1200, or CNI > 2 within CE and NE regions are highly effective in identifying tumor-containing regions in patients with

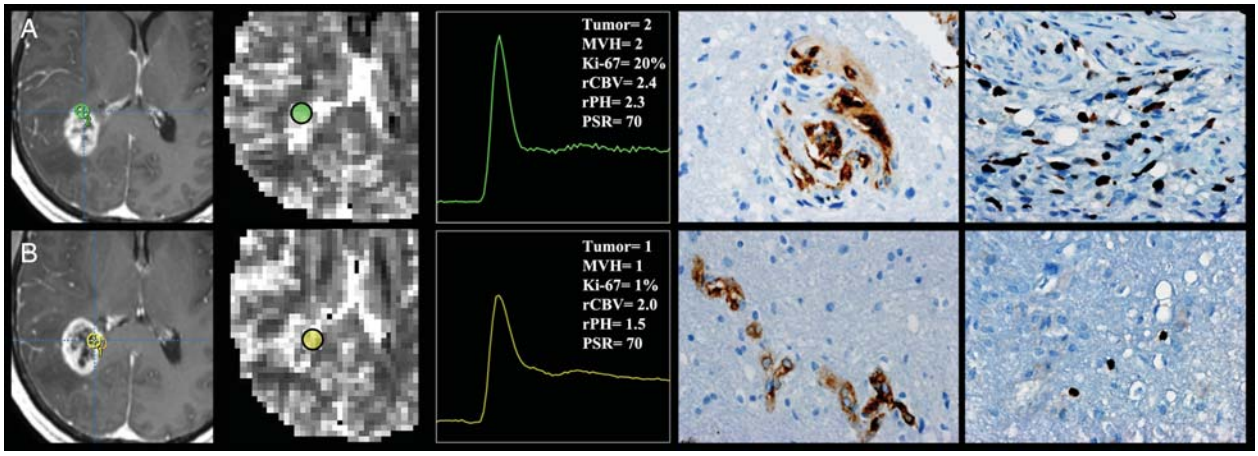

Fig. 3. Regional correlation between histopathologic features of GBM and physiologic MRI within contrast-enhancing regions. Site of 2 tumor samples (colored circles: [A] green, [B] yellow) planned on axial T1-weighted MRI (column 1), co-registered CBV maps, average dynamic ΔR2*-time curve within the tissue sample region (columns 2 and 3), and histopathologic features (column 4, microvascular hyperplasia (MVH); column 5, cellular proliferation) demonstrates significant correlation between perfusion MRI, MVH, and cellular proliferation within contrast-enhancing regions. Contrast-enhancing regions with elevated MVH and cellular proliferation (A) demonstrated elevated rCBV and rPH values (column 3) compared with similar-appearing contrast-enhancing regions that demonstrate less aggressive tumor features (B). Abbreviation: PSR, percentage of signal intensity recovery.

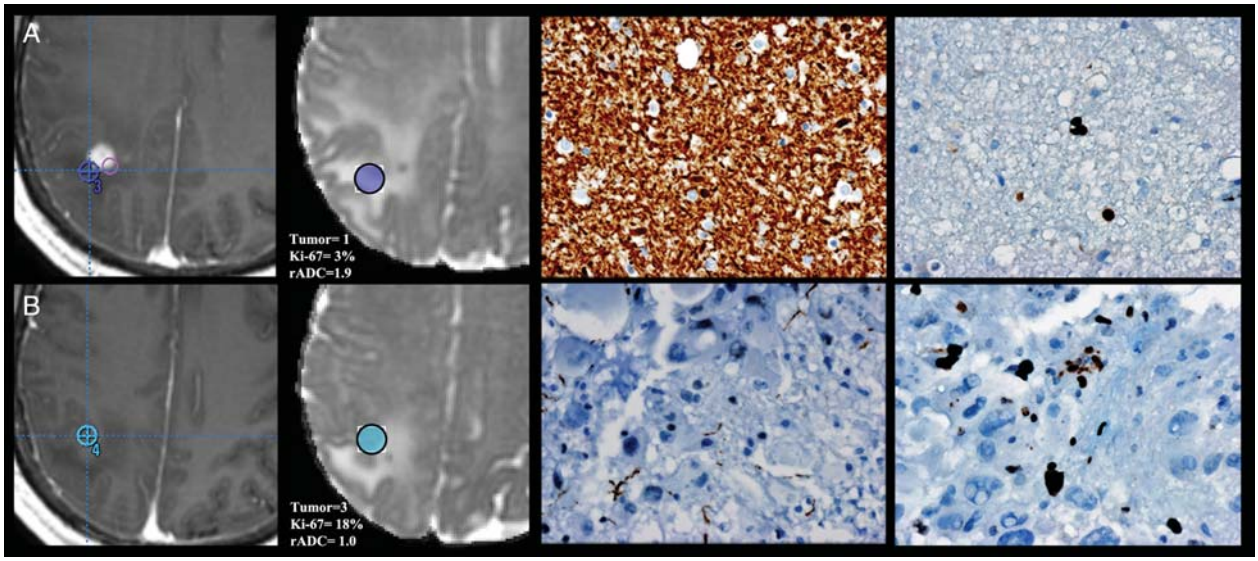

Fig. 4. Regional correlation between histopathologic features of GBM and physiologic MRI within non-enhancing regions. Site of 2 tumor samples (colored circles: [A] violet and [B] blue) planned on axial T1-weighted MRI (column 1), co-registered diffusion-weighted imaging maps (column 2), and histopathologic features (column 3, architectural disruption; column 4, cellular proliferation) demonstrates significant inverse correlation between diffusion-weighted MRI, architectural disruption, and cellular proliferation within non-enhancing regions. Non-enhancing regions with increased architectural disruption and cellular proliferation (B) demonstrated decreased rADC values (column 2) compared with similar-appearing non-enhancing regions that demonstrate less aggressive tumor features (A).

treatment-naive GBM. This is of particular interest for defining tumor burden in NE regions, where being able to distinguish reactive edema from biologically active infiltrative tumor is clinically important. Previous studies in patients with newly diagnosed GBM have shown that increased volumes of ADC < 1200 or CNI > 2 within the T2 hyperintense lesion were associated with poor overall survival prior to initial surgical resection.[41] Additionally, Saraswathy et al.[42] have demonstrated that increased volumes of these 3 physiologic MR parameters within the T2 hyperintense lesion at the post-surgery and pretreatment examinations are associated with decreased survival. Future studies will follow up on these findings by considering these measures as candidates for defining physiologic as opposed to anatomic tumor burden in serial studies of response to therapy.

From the comparison of histologic parameters within CE versus NE regions, it was clear that the hallmark

Table 4. Correlations among key histopathologic features[a]

	CE Tissue Specimen				NE Tissue Specimen			
	Tumor Score	Proliferation	Total MVH	Necrosis	Tumor Score	Proliferation	Total MVH	Necrosis
Tumor Score								
Proliferation	+				+			
Total MVH	+	+			+			
Necrosis	+	+	+		NA	NA	NA	
CA-9	+	+	+	+	NA	NA	NA	NA
AD	+	+	+	+	+	+	+	NA
TCN	+	+	+					NA
Delicate MVH	−	−	−	−				NA
Simple MVH	+	+	+	+	+	+	+	NA

Abbreviations: MVH, microvascular hyperplasia; CE, contrast-enhancing; NE, non-enhancing; +, positive correlation; −, inverse correlation; NA, not applicable; AD, architectural disruption; TCN, tumor cell number per high-power field.
[a]Statistically significant ($P < .05$) associations were observed between histopathologic features of GBM. Total MVH denotes all microvascular hyperplasia, including both simple and complex. Tumor cell density denotes mean tumor cell number per 200× microscopic field.

Table 5. Correlations among key in vivo magnetic resonance imaging parameters[a]

	CE Region				NE Region			
	rT1C	rFSE	rCBV	rADC	rT1C	rFSE	rCBV	rADC
rT1C			+			−		
rFSE				+	−			+
rCBV	+			−				−
rADC		+	−			+	−	

Abbreviations: CE, contrast-enhancing; NE, non-enhancing; rT1C, relative quantitative contrast enhancement; rFSE, relative quantitative T2 hyperintensity; rCBV, relative cerebral blood volume; rADC, relative apparent diffusion coefficient; +, positive correlation; −, inverse correlation.
[a]Statistically significant ($P < .05$) associations observed between anatomic and physiologic MRI parameters.

histopathologic features of GBM, including necrosis and complex microvascular hyperplasia, were present in a significant number of CE regions but either absent or rare in NE regions. Despite this, the majority of NE regions (81%) did contain tumor cells, as indicated by a positive tumor score. Additionally, a median Ki-67 score of 4.55% was observed among the NE regions. Interestingly, the hypoxia score was zero for all except one of the NE tumor specimens. Given that well-oxygenated tissues are sensitive to radiation damage, this finding raises the possibility that tumor in NE regions of GBM may be more effectively treated by radiation or DNA damaging chemotherapies than is tumor in CE regions. This has significant implications for planning boost volumes for radiation therapy. Of further interest in designing therapy protocols is the presence of simple microvascular hyperplasia in 65% of the samples from NE regions, which indicates that although there is increased vasculature in these areas, the vessel permeability is limited.

The relationship between increased intratumoral perfusion and malignant growth has been associated with hypoxic cellular conditions within GBM.[43–49] The morphologic feature of CE on T1-weighted MRI, which reflects the disruption of the blood–brain barrier, has previously been thought of as a marker of elevated complex microvasculature, but several studies have demonstrated a discrepancy between regions of CE and microvascular density. In this study, a strong positive correlation was observed for rCBV and rPH in CE regions with the histopathologic features of proliferation, cell density, and microvascular hyperplasia. This suggests that DSC MR imaging is capable of capturing a clinically useful, noninvasive assessment of the CE lesion for newly diagnosed GBM that can be utilized on an individual basis to provide quantifiable biomarkers.[7,12,18–21,32,50–52]

The pattern of microvascular proliferation can vary widely in GBM.[53–60] Areas of infiltrative tumor often contain delicate vasculature that resembles normal cerebral vasculature. Regions with more malignant tumor features contain both simple and complex microvascular hyperplasia. Simple microvascular hyperplasia has been characterized by hyperplastic capillaries with increased endothelial cellularity and luminal patency.[32,53–60] Complex microvascular hyperplasia is identified by large collections of capillaries with partially to completely thrombosed slit-like lumen, resulting in minimal perfusion to the surrounding tissue.[32,53–60] The correlation of rCBV and rPH with microvascular morphology suggests that DSC perfusion imaging is sensitive to all 3 types of vascular morphology and can be used to guide the acquisition of tumor samples, irrespective of the patterns of CE.

The results of our study challenge the widely held concept that T2 FSE and FLAIR hyperintense non-enhancing regions have limited malignant potential. By using physiologic MRI parameters to target tissue specimens from NE regions, we were able to identify areas with histopathologic features corresponding to biologically active tumor. Interestingly, rADC and rFSE were found to be associated with tumor score in the NE region, but this was not the case in CE regions. This

was thought to be due to partial volume averaging of tumor and necrosis within voxels that correspond to the CE region, which makes the image intensities higher than would have otherwise been observed. Previous investigations have also yielded mixed results. Sadeghi et al.,[18] in their investigation of untreated GBM, reported an inverse correlation of rADC with microvascular density but no inverse correlation between rADC and tumor cell density in their examination of 33 tumor tissue specimens. On the other hand, several other groups have reported finding an inverse correlation between rADC and cell density.[29–32] These conflicting findings are likely due to the differences in sampling strategies for obtaining tissue samples, as well as the complex interactions of water diffusivity within the heterogeneous cellular environment of GBM.

Our study was specifically designed to look at regions within the enhancing and non-enhancing lesions with physiologic imaging parameters suggestive of tumor. Given that it was not always possible to exactly target the areas requested, as well as the differences in scale of the image resolution versus the amount of tissue evaluated using histology, the fact that 90% of the enhancing samples and 81% of the non-enhancing samples had a positive tumor score is encouraging. To determine whether the imaging data can accurately define lesion boundaries would require a sampling strategy that also targeted regions of non-enhancing tumor with physiologic parameters unlikely to correspond to tumor—however, this may not be practical from the patient's perspective given the risk of taking tissue from regions of normal brain.

One limitation of this study is that the potential exists for misregistration between biopsy sites and MRI uploaded to the neuronavigational device theatrically when significant amounts of brain shift occur. Such a mismatch could lead to inaccuracy in DSC and DWI measurements—however, several steps were utilized to negate any possible brain shift that may have occurred following dural opening. We sought to minimize significant amounts of brain shift by (a) performing accurate intraoperative neuronavigational system registration to the patient's facial anatomy, (b) avoiding substantial loss of cerebrospinal fluid, (c) watching for intraoperative brain swelling, (d) testing registration accuracy against visible cortical landmarks immediately prior to biopsy sampling, and (e) using standardized ROIs of sufficient size to compensate for any minimal shift in brain location. We believe that any minimal amount of brain shift that may have occurred prior to biopsy sampling did not result in significant sampling error or adversely affect the results of this study. Further prospective studies may consider implementing the use of closed brain biopsies to negate this potential limitation.

Our investigation suggests that the heterogeneous distribution of histopathologic features within GBM can be reliably identified by physiologic MRI. The associations of imaging and histologic parameters observed indicate that these physiologic imaging variables are likely to be of interest for defining residual postsurgical tumor burden and may need to be considered in expanding the definition of the Revised Assessment in Neuro-Oncology criteria for assessing response to therapy.[61]

Conclusion

We have demonstrated that histopathologic features of GBM are differentially expressed between contrast-enhancing and non-enhancing components of the tumor. In contrast-enhancing regions, DSC perfusion MRI variables can be used to identify tissue specimens with higher tumor proliferation, necrosis, and vascular hyperplasia. In the non-enhancing component of the lesion, DWI variables are able to improve the detection of infiltrating tumor, which may lack some of the characteristic histopathologic features of GBM and may therefore respond differently to radiation or other types of therapy when compared to enhancing tissues.

Supplementary Material

Supplementary material is available at *Neuro-Oncology Journal* online (http://neuro-oncology.oxfordjournals.org/).

Acknowledgments

The first author thanks Alvin Au, King Chiu, Cynthia Cowdrey, and Bethany Barajas for their tissue processing assistance and helpful comments regarding this manuscript.

Conflict of interest statement. None declared.

Funding

National Institutes of Health [P01 CA11816-01A2].

References

1. Greenlee RT, Murray T, Bolden S. Cancer statistics 2000. *CA Cancer J Clin*. 2000;50:7–33.
2. Eby NL, Grufferman S. Increasing incidence of primary brain lymphoma in the US. *Cancer*. 1998;62:2461–2465.
3. Fulling KH, Garcia DM. Anaplastic astrocytoma of the adult cerebrum. Prognostic value of histologic features. *Cancer*. 1985;55:928–931.

4. Gilles FH, Brown WD, Leviton A. Limitations of the World Health Organization classification of childhood supratentorial astrocytic tumors. *Cancer*. 2000;88:1477–1483.
5. Prayson RA, Agamanolis DP, Cohen ML, et al. Interobserver reproducibility among neuropathologists and surgical pathologists in fibrillary astrocytoma grading. *J Neurol Sci*. 2000;175(1):33–39.
6. Coons SW, Johnson PC, Scheithauer BW, Yates AJ, Pearl DK. Improving diagnostic accuracy and interobserver concordance in the classification and grading of primary gliomas. *Cancer*. 1997;79:1381–1393.
7. Law M, Oh S, Johnson G, et al. Perfusion magnetic resonance imaging predict patient outcome as an adjunct to histopathology. *Neurosurgery*. 2006;58:1099–1107.
8. Jackson A, Kassner A, Annesley-Williams D. Abnormalities in the recirculation phase of contrast agent bolus passage in cerebral gliomas: comparison with relative blood volume and tumor grade. *Am J Neuroradiol*. 2002;23:7–14.
9. Cha S. Update on brain tumor imaging: from anatomy to physiology. *Am J Neuroradiol*. 2006;27:475–487.
10. Lev MH, Rosen BR. Clinical applications of intracranial perfusion MR imaging. *Neuroimaging Clin N Am*. 1999;9:309–331.
11. Henry RG, Vigneron DB, Fischbein NJ, et al. Comparison of relative cerebral blood volume and proton spectroscopy in patients with treated gliomas. *Am J Neuroradiol*. 2000;21:357–366.
12. Sugahara T, Korogi Y, Kochi M, et al. Correlation of MRI-determined cerebral blood volume maps with histologic and angiographic determination of vascularity of gliomas. *Am J Roentgenol*. 1998;171:1479–1486.
13. Lupo JM, Cha S, Chang SM, Nelson SJ. Dynamic susceptibility-weighted perfusion imaging of high-grade gliomas: characterization of spatial heterogeneity. *Am J Neuroradiol*. 2005;26:1446–1454.
14. Cha S, Lu S, Johnson G, Knopp EA. Dynamic susceptibility contrast MRI: correlation of signal intensity changes with cerebral blood volume measurements. *J Magn Reson Imaging*. 2000;11:114–119.
15. Cha S, Lupo JM, Chen MH, et al. Differentiation of glioblastoma multiforme and single brain metastasis by peak height and percentage of signal intensity recovery derived from dynamic susceptibility-weighted contrast-enhanced perfusion MR imaging. *Am J Neuroradiol*. 2007;28:1078–1084.
16. Barajas R, Chang J, Sneed P, Segal M, McDermott M, Cha S. Distinguishing recurrent brain metastasis from radiation necrosis following gamma knife radiosurgery using dynamic susceptibility weighted contrast-enhanced perfusion MR imaging. *Am J Neuroradiol*. 2009;30:367–372.
17. Barajas R, Chang J, Segal M, et al. Distinguishing recurrent glioblastoma multiforme from radiation necrosis following external beam radiotherapy using dynamic susceptibility weighted contrast-enhanced perfusion MRI. *Radiology*. 2009;253:486–496.
18. Sadeghi N, D'Haene N, Decaestecker C, et al. Apparent diffusion coefficient and cerebral blood volume in brain gliomas: relation to tumor cell density and tumor microvessel density based on stereotactic biopsies. *Am J Neuroradiol*. 2008;29:476–482.
19. Aronen HJ, Gazit IE, Louis DN, et al. Cerebral blood volume maps of gliomas: comparison with tumor grade and histologic findings. *Radiology*. 1994;191:41–51.
20. Cha S, Johnson G, Wadghiri YZ, et al. Dynamic, contrast-enhanced perfusion MRI in mouse gliomas: correlation with histopathology. *Magn Reson Med*. 2003;49:848–855.
21. Maia AC Jr, Malheiros SM, da Rocha AJ, et al. MR cerebral blood volume maps correlated with vascular endothelial growth factor expression and tumor grade in nonenhancing gliomas. *Am J Neuroradiol*. 2005;26:777–783.
22. Rowley HA, Grant PE, Roberts TP. Diffusion MRI: theory and applications. *Neuroimaging Clin N Am*. 1999;9:343–361.
23. Le Bihan D, Turner R, Douek P, Patronas N. Diffusion MRI: clinical applications. *Am J Roentgenol*. 1992;159:591–599.
24. Kotsenas AL, Roth TC, Manness WK, Faerber EN. Abnormal diffusion-weighted MRI in medulloblastoma: does it reflect small cell histology? *Pediatr Radiol*. 1999;29:524–526.
25. Kitis O, Altay H, Calli C, Yunten N, Akalin T, Yurtseven T. Minimum apparent diffusion coefficients in the evaluation of brain tumors. *Eur J Radiol*. 2005;55:393–400.
26. Le Bihan D, Breton E, Lallemand D, Grenier P, Cabanis E, Laval-Jeantet M. MRI of intravoxel incoherent motions: application to diffusion and perfusion in neurologic disorders. *Radiology*. 1986;161:401–407.
27. Guo AC, Cummings TJ, Dash RC, Provenzale JM. Lymphomas and high-grade astrocytomas: comparison of water diffusibility and histologic characteristics. *Radiology*. 2002;224:177–183.
28. Barajas RF Jr, Rubenstein JL, Chang JS, Hwang J, Cha S. Diffusion-weighted MRI derived apparent diffusion coefficient is predictive of clinical outcome in primary central nervous system lymphoma. *AJNR*. 2010;31:60–66.
29. Stadnik TW, Chaskis C, Michotte A, et al. Diffusion-weighted MRI of intracerebral masses: comparison with conventional MRI and histologic findings. *Am J Neuroradiol*. 2001;22:969–976.
30. Sugahara T, Korogi Y, Kochi M, et al. Usefulness of diffusion-weighted MRI with echo-planar technique in the evaluation of cellularity in gliomas. *J Magn Reson Imaging*. 1999;9:53–60.
31. Gupta RK, Cloughesy TF, Sinha U, et al. Relationships between choline magnetic resonance spectroscopy, apparent diffusion coefficient and quantitative histopathology in human glioma. *J Neurooncol*. 2000;50:215–226.
32. Barajas RF Jr, Hodgson JG, Chang JS, et al. Glioblastoma multiforme regional genetic and cellular expression patterns: influence on anatomic and physiologic MRI. *Radiology*. 2010;254(2):564–576.
33. Cha S, Johnson G, Yuz M, et al. The role of contrast-enhanced perfusion MRI in differentiating between recurrent tumor and radiation necrosis. *Proceedings: Radiological Society of North America*. 1999;213:188.
34. Cha S, Knopp EA, Johnson G, et al. Dynamic contrast-enhanced T2*-weighted MRI of recurrent malignant gliomas treated with thalidomide and carboplatin. *Am J Neuroradiol*. 2000;21:881–890.
35. Cha S, Pierce S, Knopp EA, et al. Dynamic contrast-enhanced T2*-weighted MRI of tumefactive demyelinating lesions. *Am J Neuroradiol*. 2001;22:1109–1116.
36. Sorensen AG, Buonanno FS, Gonzalez RG, et al. Hyperacute stroke: Evaluation with combined multisection diffusion-weighted and hemodynamically weighted echo-planar MRI. *Radiology*. 1996;199:391–401.
37. McKnight TR, Smith KJ, Chu PW, et al. Choline metabolism, proliferation, and angiogenesis in nonenhancing grades 2 and 3 astrocytoma. *J Magn Reson Imaging*. 2011;33(4):808–816.
38. Khayal IS, Vandenberg SR, Smith KJ, et al. MRI apparent diffusion coefficient reflects histopathologic subtype, axonal disruption, and tumor fraction in diffuse-type grade II gliomas. *Neuro Oncol*. 2011;13(11):1192–1201.

39. Lee MC, Cha S, Chang SM, Nelson SJ. Dynamic susceptibility contrast perfusion imaging of radiation effects in normal-appearing brain tissue: changes in the first-pass and recirculation phases. *J Magn Reson Imaging*. 2005;21(6):683–693.
40. Hartkens T, Rueckert D, Schnabel JA, Hawkes DJ, Hill DLG. VTK CISG Registration Toolkit: An open source software package for affine and non-rigid registration of single- and multimodal 3D images [abstract]. BVM; 2002; Leipzig, Germany: Springer-Verlag, 2002:185.
41. Crawford FW, Khayal IS, McGue C, et al. Relationship of pre-surgery metabolic and physiological MRI parameters to survival for patients with untreated GBM. *J Neurooncol*. 2009;91(3):337–351.
42. Saraswathy S, Crawford FW, Lamborn KR, et al. Evaluation of MR markers that predict survival in patients with newly diagnosed GBM prior to adjuvant therapy. *J Neurooncol*. 2009;91(1):69–81.
43. Kleihues P, Soylemezoglu F, Schäuble B, Scheithauer BW, Burger PC. Histopathology, classification, and grading of gliomas. *Glia*. 1995;15(3):211–221.
44. Preusser M, Haberler C, Hainfellner JA. Malignant glioma: neuropathology and neurobiology. *Wien Med Wochenschr*. 2006;156(11–12):332–337.
45. Tate M, Aghi M. Biology of angiogenesis and invasion in glioma. *Neurotherapeutics*. 2009;6:447–457.
46. Wong M, Prawira A, Kaye A, Hovens C. Tumour angiogenesis: Its mechanism and therapeutic implications in malignant gliomas. *J Clin Neurosci*. 2009;16:1119–1130.
47. Louis DN, Ohgaki H, Wiestler OD, Cavenee WK. World Health Organization classification of tumors: pathology and genetics of tumors of the nervous system. 4th ed. Lyon: IARC Press; 2007.
48. Knopp EA, Cha S, Johnson G, et al. Glial neoplasms: dynamic contrast-enhanced T2-weighted MRI. *Radiology*. 1999;211:791–798.
49. Brem S, Cotran R, Folkman J. Tumor angiogenesis: a quantitative method for histologic grading. *J Natl Cancer Inst*. 1972;48: 347–356.
50. Batra A, Tripathi RP, Singh AK. Perfusion magnetic resonance imaging and magnetic resonance spectroscopy of cerebral gliomas showing imperceptible contrast enhancement on conventional magnetic resonance imaging. *Australas Radiol*. 2004;48:324–332.
51. Ginsberg LE, Fuller GN, Hashmi M, et al. The significance of lack of MR contrast enhancement of supratentorial brain tumors in adults: histopathological evaluation of a series. *Surg Neurol*. 1998;49:436–440.
52. Law M, Yang S, Wang H, et al. Glioma grading: sensitivity, specificity, and predictive values of perfusion MRI and proton MR spectroscopic imaging compared with conventional MRI. *Am J Neuroradiol*. 2003;24(10):1989–1998.
53. Miyagami M, Katayama Y. Angiogenesis of glioma: evaluation of ultrastructural characteristics of microvessels and tubular bodies (Weibel–Palade) in endothelial cells and immunohistochemical findings with VEGF and p53 protein. *Med Mol Morphol*. 2005;38:36–42.
54. Deane BR, Lantos PL. The vasculature of experimental brain tumours. Part 1. A sequential light and electron microscope study of angiogenesis. *J Neurol Sci*. 1981;49:55–66.
55. Deane BR, Lantos PL. The vasculature of experimental brain tumours. Part 2. A quantitative assessment of morphological abnormalities. *J Neurol Sci*. 1981;49:67–77.
56. Rojiani AM, Dorovini-Zis K. Glomeruloid vascular structures in glioblastoma multiforme: an immunohistochemical and ultrastructural study. *J Neurosurg*. 1996;85(6):1078–1084.
57. Izycka-Swieszewska E. Immunomorphological analysis of the vascular stroma in glioblastoma. *Neurol Neurochir Pol*. 2003;37(1):59–71.
58. Wesseling P, Vandersteenhoven JJ, Downey BT, Ruiter DJ, Burger PC. Cellular components of microvascular proliferation in human glial and metastatic brain neoplasms. A light microscopic and immunohistochemical study of formalin-fixed, routinely processed material. *Acta Neuropathol*. 1993;85(5):508–514.
59. Jain R, Gutierrez J, Narang J, et al., In vivo correlation of tumor blood volume and permeability with histological and molecular angiogenic markers in gliomas. *Am J Neuroradiology*. 2011;32:388–394.
60. Jain R, Narang J, Gutierrez J, et al., Correlation of immuno-histological and perfusion vascular parameters with contrast enhancement using image-guided biopsy specimens in gliomas. *Acad Radiol*. 2011;18(8):955–962.
61. Wen PY, Macdonald DR, Reardon DA, et al. Updated response assessment criteria for high-grade gliomas: response assessment in neuro-oncology working group. *J Clin Oncol*. 2010;28(11):1963–1972.